

Photonic Weyl points due to broken time-reversal symmetry in magnetized semiconductor

Wang, Dongyang; Yang, Biao; Gao, Wenlong; Jia, Hongwei; Yang, Quanlong; Chen, Xieyu; Wei, Minggui; Liu, Changxu; Navarro-Cia, Miguel; Han, Jiaguang; Zhang, Weili; Zhang, Shuang

DOI:

[10.1038/s41567-019-0612-7](https://doi.org/10.1038/s41567-019-0612-7)

License:

None: All rights reserved

Document Version

Peer reviewed version

Citation for published version (Harvard):

Wang, D., Yang, B., Gao, W., Jia, H., Yang, Q., Chen, X., Wei, M., Liu, C., Navarro-Cia, M., Han, J., Zhang, W & Zhang, S 2019, 'Photonic Weyl points due to broken time-reversal symmetry in magnetized semiconductor', *Nature Physics*, vol. 15, no. 11, pp. 1150-1155. <https://doi.org/10.1038/s41567-019-0612-7>

[Link to publication on Research at Birmingham portal](#)

Publisher Rights Statement:

Wang, D., Yang, B., Gao, W. et al. Photonic Weyl points due to broken time-reversal symmetry in magnetized semiconductor. *Nat. Phys.* 15, 1150–1155 (2019) doi:10.1038/s41567-019-0612-7

General rights

Unless a licence is specified above, all rights (including copyright and moral rights) in this document are retained by the authors and/or the copyright holders. The express permission of the copyright holder must be obtained for any use of this material other than for purposes permitted by law.

- Users may freely distribute the URL that is used to identify this publication.
- Users may download and/or print one copy of the publication from the University of Birmingham research portal for the purpose of private study or non-commercial research.
- User may use extracts from the document in line with the concept of 'fair dealing' under the Copyright, Designs and Patents Act 1988 (?)
- Users may not further distribute the material nor use it for the purposes of commercial gain.

Where a licence is displayed above, please note the terms and conditions of the licence govern your use of this document.

When citing, please reference the published version.

Take down policy

While the University of Birmingham exercises care and attention in making items available there are rare occasions when an item has been uploaded in error or has been deemed to be commercially or otherwise sensitive.

If you believe that this is the case for this document, please contact UBIRA@lists.bham.ac.uk providing details and we will remove access to the work immediately and investigate.

1 Photonic Weyl points due to broken time-reversal symmetry in magnetized 2 semiconductor

3
4 Dongyang Wang^{1,2†}, Biao Yang^{2,3†}, Wenlong Gao², Hongwei Jia², Quanlong Yang¹, Xieyu Chen¹, Minggui Wei¹,
5 Changxu Liu², Miguel Navarro-Cía², Jiaguang Han^{1*}, Weili Zhang^{1,4*}, Shuang Zhang^{2*}
6

7 1. Center for Terahertz Waves and College of Precision Instrument and Optoelectronics Engineering, Tianjin
8 University and the Key Laboratory of Optoelectronics Information and Technology (Ministry of Education),
9 Tianjin 300072, China.

10 2. School of Physics & Astronomy, University of Birmingham, Birmingham, B15 2TT, UK

11 3. College of Advanced Interdisciplinary Studies, National University of Defense Technology, Changsha
12 410073, China.

13 4. School of Electrical and Computer Engineering, Oklahoma State University, Stillwater, Oklahoma 74078,
14 USA

15 *Correspondence to: jiaghan@tju.edu.cn; weili.zhang@okstate.edu; s.zhang@bham.ac.uk

16 †These authors contributed equally to this work.

17
18 **Weyl points are discrete locations in the three-dimensional momentum space where two bands**
19 **cross linearly with each other. They serve as the monopoles of Berry curvature in the**
20 **momentum space, and their existence requires breaking of either time-reversal or inversion**
21 **symmetry¹⁻¹⁶. Although various non-centrosymmetric Weyl systems have been reported¹⁵,**
22 **demonstration of Weyl degeneracies due to breaking of the time reversal symmetry remains**
23 **scarce and is limited to electronic systems^{17,18}. Here, we report the experimental observation of**
24 **photonic Weyl degeneracies in a magnetized semiconductor - InSb, which behaves as**
25 **magnetized plasma¹⁹ for electromagnetic waves at the terahertz band. By varying the magnetic**
26 **field strength, Weyl points and the corresponding photonic Fermi-arcs have been demonstrated.**

27 **Our observation establishes magnetized semiconductors as a reconfigurable²⁰ terahertz Weyl**
28 **system, which may prompt research on novel magnetic topological phenomena such as chiral**
29 **Majorana type edge states and zero modes in classic systems^{21,22}.**

30

31 Weyl points as topologically chiral singularity points in the three-dimensional momentum space have
32 been extensively investigated in both quantum and classical systems¹⁵. In photonics, Weyl points have
33 been observed in various systems such as gyroid photonic crystals^{7,23}, metamaterials²⁴⁻²⁶, and
34 evanescently coupled helical waveguides²⁷. However, all the previously demonstrated photonic Weyl
35 points are exclusively based on systems with broken inversion symmetry¹⁵. On the other hand, it has
36 been proposed that Weyl points due to breaking of the time-reversal symmetry may possess more
37 interesting properties such as axial anomaly, giant photocurrent and novel quantum oscillation
38 phenomena²⁸⁻³⁰. They may enable multiple striking topological features such as Majorana type edge
39 states and zero mode²², which do not exist in inversion symmetry breaking systems. Although there
40 have been theoretical proposals on implementation of Weyl degeneracies by applying external
41 magnetic fields on finely designed photonic crystals^{16,31}, very few of them are easily realizable in
42 experiment due to the challenge in three-dimensional structuring of magnetic materials^{32,33}.
43 Interestingly, it was recently theoretically proposed that plasma, the fourth fundamental state of natural
44 matter^{34,35}, can support Weyl degeneracies under external magnetic fields¹⁹, as well as nonreciprocal
45 wave transport³⁶⁻³⁸. Since there is no structuring involved, this represents a facile and tunable approach
46 for achieving photonic Weyl degeneracies arising from time-reversal symmetry breaking.

47

48 In this work, by applying magnetic field to intrinsic semiconductor InSb, we demonstrate photonic
49 Weyl points due to broken time reversal symmetry. Here InSb^{39,40} is chosen because of its very small
50 effective mass of electrons ($m^* = 0.015m_0$, where m_0 is the free electron mass) that can lead to a
51 terahertz cyclotron frequency under a moderate applied magnetic field. Along the direction of
52 magnetic field, electrons can move freely. Therefore, the dielectric function is described by the Drude
53 model, and there exists a longitudinal bulk plasma mode along the applied magnetic field. However, in
54 the plane perpendicular to the magnetic field, the dielectric function is significantly modified due to

55 the cyclotron motion of electrons, which leads to the breaking of degeneracy between the left and right
 56 circular polarizing (L/RCP) modes propagating along the magnetic field^{40,36}. The linear crossing
 57 between the longitudinal plasma mode and a circular polarizing mode forms a Weyl point in the
 58 magnetized plasma system¹⁹. By considering the coupling between the electromagnetic wave and the
 59 motion of the free charges in the plasma, we can derive a full Hamiltonian H as (see supplementary
 60 information 1)¹⁹:

$$61 \quad \omega_p \begin{bmatrix} 0 & -k \times / \sqrt{\epsilon_\infty} k_p & -i / \sqrt{\epsilon_\infty} \\ k \times / \sqrt{\epsilon_\infty} k_p & 0 & 0 \\ i \sqrt{\epsilon_\infty} & 0 & (\omega_c \Delta - i \gamma I) / \omega_p \end{bmatrix} \begin{bmatrix} E \\ H \\ V \end{bmatrix} = \omega \begin{bmatrix} E \\ H \\ V \end{bmatrix} \quad (1)$$

62 where $\omega_p = \sqrt{ne^2 / \epsilon_0 \epsilon_\infty m^*}$ and $\omega_c = eB / m^*$ are the plasma frequency and electron cyclotron
 63 frequency, respectively, with n being the free electron density, ϵ_0 the permittivity of vacuum and $\epsilon_\infty = 16$
 64 the dielectric constant at high frequencies; k_p is the vacuum wave vector at the plasma frequency, γ is
 65 the damping frequency and $\Delta = [\sigma_y, 0; 0, 0]$ with σ_y being the second Pauli matrix. By carefully
 66 controlling the temperature, the carrier density of InSb can be tuned to give a plasma frequency around
 67 $\omega_p / 2\pi = 0.3$ THz, which falls in the frequency range of our terahertz measurement setup. Depending on
 68 the relative values of ω_c and ω_p , different numbers of Weyl points may show up in our system (see
 69 supplementary information 2, Fig. S1). When $\omega_c > \omega_p$, there are two pairs of Weyl points appearing at
 70 the plasma frequency with the momentum coordinates $(k_x, k_y, k_z) = (0, 0, \pm \sqrt{\epsilon_\infty \omega_c / (\omega_c \pm \omega_p)})$,
 71 where the magnetic field is applied along z direction. Around the outer Weyl point (located at larger
 72 k_z), the first order $k \cdot p$ Hamiltonian expansion can be expressed as:

$$73 \quad H_1 = \frac{N}{2} (\sigma_0 + \sigma_3) (M \delta k_z + \xi P \delta B) + N \sigma_1 \delta k_y - N \sigma_2 \delta k_x \quad (2)$$

74 with parameters M, N, P being linear dispersion coefficients defined by the coordinates at the outer
 75 Weyl point, ξ the cyclotron constant and σ_i the Pauli matrices as described in supplementary
 76 information 3.

77

78 For a semiconductor InSb under a magnetic field strength of $B = 0.19$ T, the corresponding cyclotron
 79 frequency is $\omega_c / 2\pi \approx 0.35$ THz, which leads to the band structure shown in Fig. 1a, where plasma
 80 frequency is taken as $\omega_p / 2\pi = 0.31$ THz. Along the magnetic field, four double degenerate Weyl points

81 are located at the plasma frequency as expected. Here, we only consider the outer pair of Weyl points
82 as the inner pair with opposite topological charges are enclosed by the same equifrequency surface and
83 therefore they are not responsible for the observed topological features. Fig. 1b shows the projected
84 band structure around one of the outer Weyl points. It is shown that the dispersions of two participating
85 modes divide the momentum-energy space into four regions representing the bulk states and gaps,
86 respectively. This projected band morphology as a signature of photonic Weyl points can be observed
87 through the reflection spectra when scanning the wave vector k_z . However, in the experiment, scanning
88 k_z requires an angle resolved reflection system, which is incompatible with our magnetic terahertz
89 system. Equivalently, we can scan the magnetic field strength B instead of k_z , since they behave
90 similarly in constructing the parameter space of the Weyl point, as shown by the form of effective
91 Hamiltonian in Eq. 2. Fig. 1c shows the band structure constructed in the synthetic parameter space $[k_x,$
92 $k_y, B]$ for a fixed incident wave vector of $k_z = 2\pi/90 \text{ } \mu\text{m}^{-1}$. One can see that the linear crossing is
93 preserved in the substituted band structure (Fig. 1d, e), confirming the presence of Weyl points in the
94 synthetic parameter space (for detailed proof, see supplementary information 3).

95

96 In order to characterize the Weyl point, we apply a magnetic field along an in-plane direction (parallel
97 to the surface), as shown in Fig. 2a. It is expected that two Weyl points of opposite chiralities appear
98 along the direction of B field. They are both located outside the light cone. In order to probe the
99 reflection spectra around the Weyl points, we employ a grating to compensate the in-plane momentum
100 mismatch between the incident terahertz wave and the Weyl points. The aluminum grating, fabricated
101 directly on the surface of the InSb wafer, has a period of $p = 90 \text{ } \mu\text{m}$, a filling ratio of $2/3$ and a thickness
102 of $t = 1 \text{ } \mu\text{m}$. The sample is then placed in a low temperature environment of $T = 50 \text{ K}$ to provide a
103 plasma frequency of $\omega_p/2\pi \approx 0.31 \text{ THz}$ with a damping factor of $\gamma/2\pi = 3 \times 10^{10} \text{ Hz}$. A normal incidence
104 configuration is employed with the magnetic field applied along the grating direction, as shown in Fig.
105 2b. A high resistivity float zone Silicon 50/50 terahertz beam splitter is used for the reflection spectra
106 measurement (refer to Methods). The grating provides a fundamental order wave vector of magnitude
107 $G = 2\pi/p$ to excite both the bulk and surface states supported by the magnetized InSb. As the magnetic
108 field strength is scanned from 0-1 Tesla, we measure the reflection spectrum. These measurements

109 provide the projected band information as shown in Fig. 2c, where the band crossing can be clearly
110 observed at the frequency of $\omega_p/2\pi = 0.31$ THz and magnetic field of $B = 0.19$ T. Fig. 2d shows the
111 corresponding full wave simulation results that take into account the actual dissipation in the
112 magnetized plasma. Simulation results shown in Fig. 2d show good agreement with the experimental
113 results. On the other hand, when the grating direction is rotated away from the direction of magnetic
114 field, the crossing point disappears and a bandgap is formed, as shown in supplementary information 4,
115 Fig. S2. The experimental results confirm the presence of Weyl degeneracies in a magnetized
116 semiconductor system.

117

118 The most important signature of a Weyl system is the presence of Fermi-arcs. The photonic Fermi-arcs
119 in the original momentum space are explored in the supplementary information 5 where the surface
120 states are found to be separated into two separated frequency bands: $\omega < \omega_p$ and $\omega > \sqrt{\omega_p^2 + \omega_c^2}$ with
121 opposite signs of k_y , respectively, due to the magnetic field induced cyclotron resonance. These two
122 branches of surface states are observed in the experimentally measured f - B plot manifested as
123 absorption lines in the reflection spectra. The theoretically calculated surface states are indicated by a
124 black dashed line in both the experimental and simulated results in Fig. 2c-d, which fits well with the
125 corresponding surface states induced absorption.

126

127 To further explore the surface state features in the magnetized Weyl system, a second experimental
128 configuration is employed as shown in Fig. 3a, in which the incidence terahertz beam and the applied
129 magnetic field are arranged to form angles $\theta = 45^\circ$ and $\alpha = 45^\circ$ with respect to the sample normal and
130 sample surface, respectively. In this configuration, a beam splitter is not required and therefore the
131 signal noise ratio of the measurement is improved by approximately four times in comparison to that of
132 normal incidence. Rotating the grating around x axis by an angle of φ as shown in Fig. 3a (bottom-left
133 inset) provides a non-zero k_y to excite the off k_z axis surface states on the k_y - k_z plane, as shown in Fig.
134 3a (right insets). Meanwhile, due to the tilted incidence, the degeneracy between $\pm 1^{\text{st}}$ grating order is
135 lifted. The $\pm 1^{\text{st}}$ order excitation wave vector is given by $[k_y, k_z]_{\pm 1} = [\pm G \sin\varphi, \pm G \cos\varphi + k_0 \sin 45^\circ]$ as
136 illustrated in Fig. 3a (bottom-left inset), where φ is the angle formed between the grating momentum

137 and z axis. For a given magnetic field, it is expected that the $\pm 1^{\text{st}}$ order with opposite signs of k_y , can
138 excite surface states at the two aforementioned frequency bands (see supplementary information 5, Fig
139 S3).

140

141 In this tilted configuration, the Weyl points are projected onto the sample surface with a smaller
142 in-plane wave vector ($k_x = \pm \sqrt{\epsilon_\infty \omega_c / 2(\omega_c - \omega_p)}$), as shown in Fig. 3b. A different sample with a
143 greater grating periodicity of $p = 120 \mu\text{m}$ is therefore designed to match the momentum. The new
144 sample has a similar plasma frequency $\omega_p / 2\pi \approx 0.31 \text{ THz}$ as the previous one. The projected bulk
145 bands on $B - f$ plane are plotted for $\varphi = -30^\circ$ and -45° in Fig. 3c and f, where the bulk states excited by
146 the $\pm 1^{\text{st}}$ grating orders have a large overlap with each other and are indicated by navy and purple color,
147 respectively. The surface states excited by the $\pm 1^{\text{st}}$ grating orders are also calculated and shown in Fig.
148 3c and f, respectively. At each grating angle φ , the $\pm 1^{\text{st}}$ order excitations with opposite signs of k_y , form
149 two separate branches, which merge into each other at zero applied magnetic field B . It is also
150 observed that at increasing φ , the angle between two surface state branches widens, due to the increase
151 in the slopes of the dispersion. It can be noticed that the surface state is interrupted around the
152 cyclotron position, which is caused by the strong cyclotron resonance that leads to relatively high
153 reflection⁴¹. For a negative φ , the diffraction orders that excite the two surface state branches switch in
154 comparison to that with a positive φ (see more discussion in supplementary information 6, Fig. S4).

155

156 The measured reflection spectra are shown in Fig. 3e and Fig. 3h for $\varphi = -30^\circ$ and -45° (see
157 supplementary information 7, Fig. S5 for more measured results), respectively, which presents the
158 superposed band projection for both bulk and surface states. The corresponding simulation results for
159 the reflection spectra shown in Fig. 3d and g are in good agreement with the experiment results. It is
160 noticed that there exists a cut-off for the surface state branch at higher frequencies, due to the limited
161 momentum provided by the grating (see supplementary information 8, Fig. S6). Higher grating orders
162 are also excited in the experiment, which contribute to the absorptions along the surface state branch at
163 the higher frequencies beyond the cut-off of the first grating order.

164

165 For a given grating diffraction order, the projection of photonic Weyl point can also be described in the
166 parameter space $[\varphi, B]$. Using the same configuration as in Fig. 3a, a sample with higher plasma
167 frequency of $\omega_p/2\pi \approx 0.53$ THz and grating periodicity of $p=150\mu\text{m}$ is measured (supplementary
168 information 9, Fig. S7). The Weyl point which is projected at location $(k_y, k_z) = (0, G + k_0 \sin 45^\circ)$ in the
169 momentum space turns into $(\varphi, B) = (0, 0.472)$ for the +1st grating order (supplementary information
170 10, Fig. S8). The projected dispersion of the bulk states with respect to B for $\varphi = 0$ is shown in Fig. 4a,
171 where a linear crossing indicating an effective Weyl point is observed. The linear dispersion with
172 respect to φ around the effective Weyl point is confirmed in Fig. 4b. The calculated surface states for
173 different grating orientation angle φ are shown in Fig. 4c and d, where it is clearly shown that larger
174 orientation angles lead to steeper dispersion in B . A photonic Fermi-arc in the B - φ plane can thus be
175 constructed at a given frequency. For the +1st grating order excitation, the photonic Fermi-arcs together
176 with the bulk bands at two different frequencies 0.46 THz and 0.6 THz are shown in Fig. 4e and f,
177 respectively. The experimental data (cyan hollow dots) are in good agreement with the theoretical
178 result. The small deviation between measurements and theory may arise from the nonlocal effect, i.e.
179 spatial dispersion, of the material^{42,43}. It should be noted that due to the presence of loss, the Weyl
180 point transforms into exceptional ring¹⁹, which possesses the same topological charge as a Weyl
181 point. The size of the ring is calculated based on the actual dissipation of the semiconductor and is
182 found to be negligibly small (see supplementary information 11, Fig. S9). Meanwhile, a discussion of
183 the loss and surface wave resonance is shown in supplementary information 12, Fig. S10.

184

185 The demonstrated time-reversal breaking Weyl points in magnetized plasma will promote the
186 investigation of topological phases in magnetoplasmon²², where classical chiral Majorana edge states
187 and zero modes have been proposed. Moreover, by introducing spatially variant magnetic field or
188 temperature, synthetic gauge potential can be realized, which may enable observation of other
189 topological exotic effects, such as chiral⁴⁴ and gravitational⁴⁵ anomaly, which are initially investigated
190 in high energy physics and astrophysics. The observed Weyl points and topological surface states in
191 the magnetized InSb also represent the first demonstration of topological phases in the terahertz band,
192 which may facilitate the development of terahertz topological devices.

193

194 **Methods:**

195 The low temperature and high magnetic field environment are provided by a liquid Helium based
196 commercial SpectroMag system from Oxford Instruments. The magnetic field is generated by a
197 superconducting coil with controllable electric current, and the temperature can be controlled by
198 adjusting the heater power to balance with the liquid helium cooling circulation. Four terahertz (THz)
199 transparent windows are embedded in the system for spectrum characterization. A fixed magnetic field
200 direction is aligned to be along two opposite windows and allows for both Faraday and Voigt
201 configuration. A fiber based THz time-domain spectroscopy (TDS) system is used for the terahertz
202 reflection measurement and the THz antennas can be freely arranged to fit with the experimental
203 configuration. The THz beam from transmitter antenna was focused onto the sample with a THz lens
204 and the reflected wave was collected and delivered to the receiver antenna with another lens in the
205 tilted incidence configuration. For the normal incidence case, a 50/50 beam splitter is arranged to
206 redirect the reflected THz wave. The THz beam width is around 5-8mm at the sample surface and the
207 sample size is 15mm×15mm.

208

209 For the THz TDS measurement, both the sample and reference signals are acquired. The reflection
210 signal of samples at room temperature $T=300\text{K}$ is taken as the reference, with InSb acting as metal for
211 THz wave to achieve total reflection of incident THz wave. A time delay range of 100ps after the main
212 THz pulse is scanned for both the sample and reference signals, which corresponds to a frequency
213 resolution of 10GHz. The Fourier-transformed signal of sample is normalized with the reference to
214 give the reflection spectrum. During the measurement, the magnetic field is scanned with a step size of
215 0.01Tesla, so that the reflection spectra on f - B plane can be obtained. In order to reduce the effect of
216 Fabry-Perot resonance between top and bottom surface of InSb, the measured sample ($h=625\ \mu\text{m}$) is
217 attached with another bare InSb substrate (cut from the same InSb wafer) at the bottom to achieve a
218 sample thickness of $h=1250\ \mu\text{m}$, as described in the main text.

219

220 The simulation is carried out with the ‘frequency domain solver’ module of the commercial software

221 CST microwave studio. In the simulation, the InSb substrate is modeled as gyrotropic dispersion
222 material.

223

224 **Data Availability**

225 The data that support the findings of this study are available from the corresponding authors upon
226 reasonable request.

227

228 **Acknowledgement**

229 We thank Zhenwei Zhang and Cunlin Zhang at Capital Normal University for experiment instrument
230 support. This work is supported by the European Research Council Consolidator Grant
231 (TOPOLOGICAL), Horizon 2020 Action Project grant 734578 (D-SPA) and 777714 (NOCTORNO),
232 EPSRC GrantNo. EP/J018473/1, and the National Science Foundation of China (Grant Nos. 61875150
233 and 61420106006). S.Z. acknowledges support from the Royal Society and Wolfson Foundation. M.
234 N.-C. acknowledges support from University of Birmingham (Birmingham Fellowship), EPSRC
235 (grant No. EP/S018395/1) and the Royal Society (grant No. IES/R3/183131).

236

237 **Author Contributions**

238 D.W., B.Y. and S.Z. initiated the project and designed the experiment. D.W., Q.Y., X.C., M.W. and J.H.
239 fabricated samples. D.W. and J.H. carried out the measurement. D.W., B.Y., J.H., W.Z. and S.Z.
240 analyzed data. D.W., B.Y., W.G., H.J., M.N.-C. and C.L. performed simulations. D.W., B.Y., W.G.,
241 M.N.-C., J.H., W.Z. and S.Z. provided the theoretical explanations. J.H., W.Z. and S.Z. supervised the
242 project. All authors discussed the results and contributed to the final manuscript.

243

244 **Figure captions:**

245

246 **Figure 1 | Bulk states of lossless magnetized InSb.** **a**, The band structure and Weyl points in
247 magnetized plasma system. The parameters used in the calculation are: $\omega_p/2\pi = 0.31$ THz, $B = 0.19$ T
248 and no damping is considered. **b**, Band projection around the outer Weyl point, whose coordinate is $(k_x,$
249 $k_y, k_z) = (0, 0, 10.8) k_p$ with k_p indicating the vacuum wave vector at plasma frequency. **c**, Band
250 structure with k_z been substituted by B . A fixed value of $k_z = 10.8 k_p$ is assumed and the magnetic field
251 scanning range is $0 \leq B \leq 1$ T. **d**, Dispersion along B around the outer Weyl point in **c**. **e**, Similar to **d** but
252 along $k_{x(y)}$. k_0 indicates vacuum wave vector.

253

254 **Figure 2 | Observation of terahertz Weyl point in a magnetized semiconductor system.** **a**,
255 Schematic of the sample with metal grating on top of the InSb substrate. The specified magnetic field
256 direction is along grating, geometric parameters are: $p = 90 \mu\text{m}$, $h = 1250 \mu\text{m}$ and $t = 1 \mu\text{m}$. **b**,
257 Illustration of the experiment setup for terahertz reflection measurement. Two terahertz antennas are
258 placed to be right angle and form a normal incidence onto the sample. 'BS' indicates the 50/50 beam
259 splitter. The sample is placed in a commercial equipment with low temperature environment, where
260 the built in superconducting coils provide tunable magnetic field strength. Linear polarization of
261 incidence wave is indicated. **c**, Experimentally measured reflection spectra. The band crossing
262 coordinate can be estimated as $\omega_p/2\pi \approx 0.31$ THz and $B = 0.19$ T. **d**, Reflection spectra calculated with
263 full wave simulation, a damping factor of $\gamma/2\pi = 3 \times 10^{10}$ Hz is considered in the simulation. Red/blue
264 curves are the bulk states and black curves are surface states under lossless assumption, respectively.

265

266 **Figure 3 | Surface states under tilted incidence excitation.** **a**, Schematic experiment configuration
267 with respect of $\theta=45^\circ$ and $\alpha=45^\circ$. The rotation angle of grating is φ about x -axis. $\pm 1^{\text{st}}$ grating order
268 momentum is coupled with incidence wave and excites surface states for corresponding grating angle
269 φ . The material parameters for the sample are $\omega_p/2\pi \approx 0.31$ THz and $\gamma/2\pi = 3 \times 10^{10}$ Hz. **b**, Projected
270 Weyl points on the sample surface plane. **c**, $\pm 1^{\text{st}}$ grating order excited bulk bands within the range of k_x

271 $\in [-100k_0, 100k_0]$ ($+1^{\text{st}}$ bands are indicated with navy color and -1^{st} with purple) and surface states for
272 $\varphi = 30^\circ$ on the $B - f$ plane. Here we set $\gamma = 0$. **d**, Simulated reflection spectra for $\varphi = 30^\circ$, $h=10\text{mm}$, as
273 well as the calculated surface states (black dashed) under $\pm 1^{\text{st}}$ grating order excitation. **e**,
274 Experimentally measured reflection spectra for $\varphi = 30^\circ$, $h=1250 \mu\text{m}$. **f-h**, Similar to **c-e** but for $\varphi = 45^\circ$.
275

276 **Figure 4 | Photonic Weyl points and Fermi-arcs in the synthetic space.** **a**, Projected band along k_x
277 axis on the $f - B$ plane, within the range of $k_x \in [-100k_0, 100k_0]$ for $\varphi=0^\circ$, the Weyl point can be found
278 around $B=0.472 \text{ T}$. **b**, The linear dispersion along φ . **c**, $\pm 1^{\text{st}}$ order grating selected surface state on $B - f$
279 plane for $\varphi=-30^\circ$, -45° , -60° . **d**, Similar to **c** but for $\varphi=30^\circ$, 45° , 60° . **e**, Constructed photonic
280 Fermi-arcs on (B, φ) space for frequency of $f=0.46 \text{ THz}$, within the range of $k_x \in [-100k_0, 100k_0]$. **f**,
281 Similar to **e** but for $f=0.6 \text{ THz}$. Cyan hollow dots indicate experimentally measured results.
282

283 **References:**

- 284 1 Wan, X., Turner, A. M., Vishwanath, A. & Savrasov, S. Y. Topological semimetal and Fermi-arc surface states in
285 the electronic structure of pyrochlore iridates. *Physical Review B* **83**, 205101 (2011).
- 286 2 Burkov, A. A. & Balents, L. Weyl Semimetal in a Topological Insulator Multilayer. *Physical Review Letters* **107**,
287 127205 (2011).
- 288 3 Xu, G., Weng, H., Wang, Z., Dai, X. & Fang, Z. Chern Semimetal and the Quantized Anomalous Hall Effect in
289 HgCr₂Se₄. *Physical Review Letters* **107**, 186806 (2011).
- 290 4 Lu, L., Fu, L., Joannopoulos, J. D. & Soljačić, M. Weyl points and line nodes in gyroid photonic crystals. *Nature*
291 *Photonics* **7**, 294-299 (2013).
- 292 5 Xu, S.-Y. *et al.* Discovery of a Weyl fermion semimetal and topological Fermi arcs. *Science* **349**, 613-617 (2015).
- 293 6 Weng, H., Fang, C., Fang, Z., Bernevig, B. A. & Dai, X. Weyl Semimetal Phase in Noncentrosymmetric
294 Transition-Metal Monophosphides. *Physical Review X* **5**, 011029 (2015).
- 295 7 Lu, L. *et al.* Experimental observation of Weyl points. *Science* **349**, 622-624 (2015).
- 296 8 Soluyanov, A. A. *et al.* Type-II Weyl semimetals. *Nature* **527**, 495-498 (2015).
- 297 9 Huang, L. *et al.* Spectroscopic evidence for a type II Weyl semimetallic state in MoTe₂. *Nature Materials* **15**,
298 1155-1160 (2016).
- 299 10 Lin, Q., Xiao, M., Yuan, L. & Fan, S. Photonic Weyl point in a two-dimensional resonator lattice with a synthetic
300 frequency dimension. *Nature Communications* **7**, 13731 (2016).
- 301 11 Chang, G. *et al.* Room-temperature magnetic topological Weyl fermion and nodal line semimetal states in
302 half-metallic Heusler Co₂TiX (X=Si, Ge, or Sn). *Scientific Reports* **6**, 38839 (2016).
- 303 12 Wang, Z. *et al.* Time-Reversal-Breaking Weyl Fermions in Magnetic Heusler Alloys. *Physical Review Letters* **117**,
304 236401 (2016).
- 305 13 Kübler, J. & Felser, C. Weyl points in the ferromagnetic Heusler compound Co₂MnAl. *EPL (Europhysics Letters)*
306 **114**, 47005 (2016).
- 307 14 Wang, Q., Xiao, M., Liu, H., Zhu, S. & Chan, C. T. Optical Interface States Protected by Synthetic Weyl Points.
308 *Physical Review X* **7**, 031032 (2017).
- 309 15 N.P. Armitage, E. J. M., Ashvin Vishwanath. Weyl and Dirac semimetals in three-dimensional solids. *Reviews of*
310 *Modern Physics* **90**, 015001 (2018).
- 311 16 Ozawa, T. *et al.* Topological photonics. *Reviews of Modern Physics* **91**, 015006 (2019).
- 312 17 Borisenko, S. *et al.* Time-Reversal Symmetry Breaking Type-II Weyl State in YbMnBi₂. Preprint at
313 <https://arxiv.org/abs/1507.04847> (2015).
- 314 18 Liu, E. *et al.* Giant anomalous Hall effect in a ferromagnetic kagome-lattice semimetal. *Nature Physics* **14**,
315 1125-1131 (2018).
- 316 19 Gao, W. *et al.* Photonic Weyl degeneracies in magnetized plasma. *Nature Communications* **7**, 12435 (2016).
- 317 20 Cheng, X. *et al.* Robust reconfigurable electromagnetic pathways within a photonic topological insulator.
318 *Nature Materials* **15**, 542-548 (2016).
- 319 21 Tan, W., Chen, L., Ji, X. & Lin, H.-Q. Photonic simulation of topological superconductor edge state and
320 zero-energy mode at a vortex. *Scientific Reports* **4**, 7381 (2014).
- 321 22 Jin, D. *et al.* Topological magnetoplasmon. *Nature Communications* **7**, 13486 (2016).
- 322 23 Goi, E., Yue, Z., Cumming, B. P. & Gu, M. Observation of Type I Photonic Weyl Points in Optical Frequencies.
323 *Laser & Photonics Reviews* **12**, 1700271 (2018).

324 24 Chen, W.-J., Xiao, M. & Chan, C. T. Photonic crystals possessing multiple Weyl points and the experimental
325 observation of robust surface states. *Nature Communications* **7**, 13038 (2016).

326 25 Yang, B. *et al.* Direct observation of topological surface-state arcs in photonic metamaterials. *Nature*
327 *Communications* **8**, 97 (2017).

328 26 Yang, B. *et al.* Ideal Weyl points and helicoid surface states in artificial photonic crystal structures. *Science* **359**,
329 1013-1016 (2018).

330 27 Noh, J. *et al.* Experimental observation of optical Weyl points and Fermi arc-like surface states. *Nature Physics*
331 **13**, 611-617 (2017).

332 28 O'Brien, T. E., Diez, M. & Beenakker, C. W. J. Magnetic Breakdown and Klein Tunneling in a Type-II Weyl
333 Semimetal. *Physical Review Letters* **116**, 236401 (2016).

334 29 Liu, C.-X., Ye, P. & Qi, X.-L. Chiral gauge field and axial anomaly in a Weyl semimetal. *Physical Review B* **87**,
335 235306 (2013).

336 30 Kharzeev, D. E., Kikuchi, Y., Meyer, R. & Tanizaki, Y. Giant photocurrent in asymmetric Weyl semimetals from the
337 helical magnetic effect. *Physical Review B* **98**, 014305 (2018).

338 31 Yang, Z. *et al.* Weyl points in a magnetic tetrahedral photonic crystal. *Opt. Express* **25**, 15772-15777 (2017).

339 32 Wang, Z., Chong, Y., Joannopoulos, J. D. & Soljačić, M. Observation of unidirectional backscattering-immune
340 topological electromagnetic states. *Nature* **461**, 772-775 (2009).

341 33 Poo, Y., Wu, R.-x., Lin, Z., Yang, Y. & Chan, C. T. Experimental Realization of Self-Guiding Unidirectional
342 Electromagnetic Edge States. *Physical Review Letters* **106**, 093903 (2011).

343 34 Morozov, A. I. *Introduction to Plasma Dynamics*. (CRC Press, Boca Raton, 2012).

344 35 Zhang, S., Xiong, Y., Bartal, G., Yin, X. & Zhang, X. Magnetized Plasma for Reconfigurable Subdiffraction Imaging.
345 *Physical Review Letters* **106**, 243901 (2011).

346 36 Yang, B., Lawrence, M., Gao, W., Guo, Q. & Zhang, S. One-way helical electromagnetic wave propagation
347 supported by magnetized plasma. *Scientific Reports* **6**, 21461 (2016).

348 37 Gangaraj, S. A. H. & Monticone, F. Topological waveguiding near an exceptional point: defect-immune,
349 slow-light, and loss-immune propagation. *Physical review letters* **121**, 093901 (2018).

350 38 Hassani Gangaraj, S. A. *et al.* Unidirectional and diffractionless surface plasmon polaritons on
351 three-dimensional nonreciprocal plasmonic platforms. *Physical Review B* **99**, 245414 (2019).

352 39 Howells, S. C. & Schlie, L. A. Transient terahertz reflection spectroscopy of undoped InSb from 0.1 to 1.1 THz.
353 *Applied Physics Letters* **69**, 550-552 (1996).

354 40 Wang, X., Belyanin, A. A., Crooker, S. A., Mittleman, D. M. & Kono, J. Interference-induced terahertz
355 transparency in a semiconductor magneto-plasma. *Nature Physics* **6**, 126-130 (2009).

356 41 Zhang, Q. *et al.* Superradiant decay of cyclotron resonance of two-dimensional electron gases. *Physical review*
357 *letters* **113**, 047601 (2014).

358 42 Buddhiraju, S. *et al.* Absence of unidirectionally propagating surface plasmon-polaritons in nonreciprocal
359 plasmonics. Preprint at <https://arxiv.org/abs/1809.05100> (2018).

360 43 Hassani Gangaraj, S. A. & Monticone, F. Do Truly Unidirectional Surface Plasmon-Polaritons Exist? , Preprint at
361 <https://arxiv.org/abs/1904.08392> (2019).

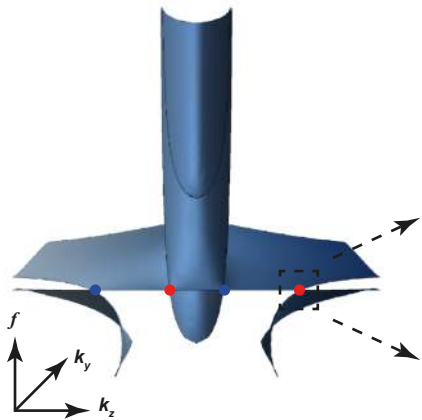
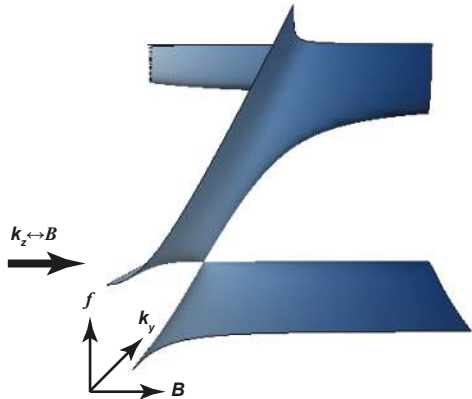
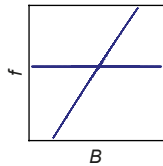
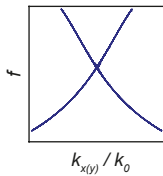
362 44 Jia, H. *et al.* Observation of chiral zero mode in inhomogeneous three-dimensional Weyl metamaterials. *Science*
363 **363**, 148-151 (2019).

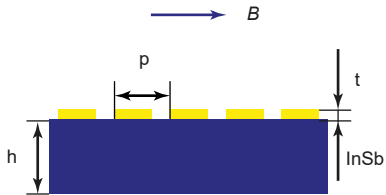
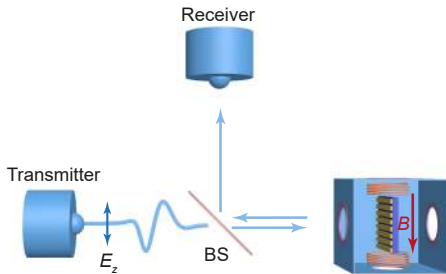
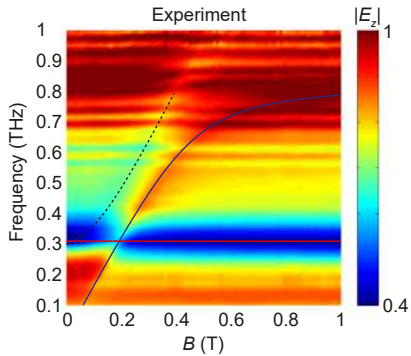
364 45 Gooth, J. *et al.* Experimental signatures of the mixed axial-gravitational anomaly in the Weyl semimetal NbP.
365 *Nature* **547**, 324-327 (2017).

366

367

368

a**b****c****d****e**

a**b****c****d**